MATERIALS CHEMISTRY FRONTIERS

RESEARCH ARTICLE

View Article Online
View Journal | View Issue

Cite this: *Mater. Chem. Front.*, 2024, **8**, 3331

Mechanochromic hydrogen-bonded cocrystals with a salient effect upon heating†

Armando Navarro-Huerta,[a] Antonio Juárez-Calixto,[a] María Eugenia Sandoval-Salinas,[b] Yoarhy A. Amador-Sánchez,[c] Joelis Rodríguez-Hernández,[d] Alejandra Núñez-Pineda,[ae] Mario Rodríguez,[f] Rachel Crespo-Otero[b] and Braulio Rodríguez-Molina*[a]

Received 22nd May 2024,
Accepted 13th August 2024

DOI: 10.1039/d4qm00421c

rsc.li/frontiers-materials

Herein, we report the characterization of two hydrogen-bonded cocrystals, termed **AC-TFTA** and **AC-PFBA**, with mechanofluorochromism upon grinding. The heating of single crystals of **AC-TFTA** promotes microscopic displacements due to a decarboxylation process, which was studied through calorimetry-based techniques, gas chromatography/mass spectrometry, and hot-stage microscopy. Using solid-state nuclear magnetic resonance (ssNMR), powder X-ray diffraction (PXRD), and UV-Vis/fluorescence spectroscopy, we demonstrated that **AC-TFTA** displays sharper photophysical changes than its analog **AC-PFBA**, attributable to differences in the energies of their non-covalent interactions. Furthermore, the reversibility of the amorphous phase in both cocrystals was explored. However, fatigue tests led us to conclude that **AC-TFTA** displays potential for application as an anticounterfeiting agent, in contrast with the more robust crystalline **AC-PFBA**. This work emphasizes the importance of cocrystallization in generating accessible and functional mechanofluorochromic materials.

1. Introduction

The quest for smart materials capable of dynamically responding to an external stimulus has led to significant advancements in materials science and engineering. Among these responsive materials, mechanofluorochromic (MFC) compounds have emerged as promising candidates due to their ability to undergo reversible changes in their fluorescence emission under mechanical stress.[1,2] Their expanding array of applications, ranging from anticounterfeiting to ref. 3 encoding,[4] sensing,[5] and other emissive applications,[6] has attracted considerable interest in recent years.

Frequently reported mechanofluorochromic compounds are based on boranyls,[7,8] tetraphenylethylene compounds,[9–11] benzimidazole-like skeletons[12,13] and cyanovinylethylene acceptors.[14] In addition, gold-containing cyano-based small molecules and other inorganic materials can display these attractive properties.[15–20]

A typical methodology for developing MFC materials involves the amalgamation of electron-donating and electron-withdrawing functional groups in one molecule *via* covalent bonds. Such a combination allows for specific modulation of the resulting frontier molecular orbitals (FMOs) and causes a red-shift in the photoluminescence (PL) properties.[21]

The use of bulky and twisted conjugated components also helps to obtain MFC compounds because the grinding process tends to modify the dihedral angles of the moieties with respect to the backbone, thus provoking changes in the π-conjugation and impacting the optical properties of the materials.[9] When the structural variations are drastic, they may lead to changes from one solid form to another, whether in a single-crystal to single-crystal (SCSC) transition,[22] or from a crystalline to an amorphous material,[23] among other possibilities.

Including the mentioned features in a single molecule could be synthetically challenging and potentially lead to low yields, quenched emission, or minimal solubility of the resulting compounds. To overcome the cited limitations, several groups have relied on the principles of crystal engineering and

[a] *Instituto de Química, Universidad Nacional Autónoma de México, Circuito Exterior S/N Ciudad Universitaria, Coyoacan 04510, Mexico City, Mexico. E-mail: brodriguez@iquimica.unam.mx*
[b] *UCL Department of Chemistry, London WC1H 0AJ, UK*
[c] *Laboratorio de Fisicoquímica y Reactividad de Superficies (LaFReS), Instituto de Investigaciones en Materiales, Universidad Nacional Autónoma de México, Circuito Exterior S/N Ciudad Universitaria, Coyoacán 04510, Mexico City, Mexico*
[d] *Centro de Investigación en Química Aplicada (CIQA), Boulevard Enrique Reyna Hermosillo No. 140, Saltillo 25294, Coahuila, Mexico*
[e] *Centro Conjunto de Investigación en Química Sustentable (CCIQS) UAEM-UNAM, Carretera Toluca-Atlacomulco Km 14.5, Toluca, Estado de México, Mexico*
[f] *Research Group of Optical Properties of Materials (GPOM), Centro de Investigaciones en Óptica, CIO, Apdo. Postal 1-948, 37000 León, Guanajuato, Mexico*

† Electronic supplementary information (ESI) available: Synthetic and experimental procedures, spectroscopic data (NMR, FTIR, HRMS), VT ssNMR spectra, final crystallographic refinement parameters, PXRD diffractograms, Hirshfeld surface maps, DFT computational details and ESR spectra. CCDC 2351862–2351865. For ESI and crystallographic data in CIF or other electronic format see DOI: https://doi.org/10.1039/d4qm00421c

supramolecular chemistry using cocrystallization as the preferred approach to enable modifications of the photoluminescence of solids.[24–26] Molecular cocrystals are multicomponent solids composed of neutral, crystalline molecules in specific stoichiometric ratios, termed coformers.[27] Its development has enhanced the control of physicochemical properties, for instance solubility, thermal/photo stability and its photophysical properties, owing to the availability of synthetic methods and commercial coformers.[28]

Interestingly, the research of crystalline MFC materials based on cocrystallization is scarce.[29–31] In this context, the hydrogen bond, a directional, strong, non-covalent interaction, has been a pivotal area of study due to the robustness that it can provide to crystalline solids. Notable examples of these compounds are the works of Ito,[32] Xie,[33] and Dar,[34,35] who have successfully developed crystalline materials with high responsiveness and multicolor emission.

The multi-responsiveness of crystalline materials is not limited to the stress-induced stimuli but includes the thermal treatment of crystalline samples that can lead to macroscopic displacements due to the release of molecules, such as carbon dioxide.[36] In the context of cocrystals, Gong *et al.* reported the jumping mechanism of a coronene-TFBQ cocrystal triggered by the expelling of the acceptor molecule in a thermal stimulus.[37] More recently, Das *et al.* reported a salt formed by piperazine-trifluoroacetic acid where the crystals released TFA molecules upon bending.[38]

Considering the above, we envisioned using a fused carbazole-acridine fragment as the hydrogen bond acceptor due to its straightforward synthesis, thermal robustness, and photoluminescent properties. Complementarily, we draw on perfluorobenzoic and tetrafluoroterephthalic acids to facilitate new crystalline forms and possible responsiveness inspired by previous reports.[33,39,40] It is important to note that additional non-classic hydrogen bonds may also enable interesting properties both in the strength and lattice responsiveness of the crystalline packing.[5,41]

Here, we report the systematic characterization of two hydrogen-bonded cocrystals with 1 : 1 (**AC-PFBA**) or 2 : 1 (**AC-TFTA**) stoichiometries. The properties of each solid were thoroughly explored and characterized by single crystal and powder X-ray diffraction, fluorescence, UV spectroscopy, and variable temperature solid-state NMR. Remarkably, the heating process of **AC-TFTA** is translated into jumping of its single crystals, which were successfully correlated with a decarboxylation of the TFTA moiety. Further experiments with this cocrystal revealed its potential application in anticounterfeiting due to the remarkable color change between ground and crystalline phases upon heating and vapor exposure.

2. Experimental section

Reagents and solvents were purchased from the company Sigma-Aldrich®. Reactions were monitored through TLC using silica gel plates 60 F_{254} purchased from Merck®. Spots were detected by UV-light absorption. Reactions were carried out in an inert atmosphere using nitrogen (N_2). Solution ^{1}H and ^{13}C experiments were recorded at room temperature using a Jeol Eclipse 270. The spectroscopic data is referenced to $CDCl_3$ (^{1}H: δ = 7.26 ppm, s; ^{13}C: δ = 77.0 ppm). High-resolution mass spectrometry was obtained in a Jeol JMS-AccuTOF JMS-T100LC spectrometer, ionization mode: direct analysis in real time (DART). FTIR-ATR spectra experiments were recorded with Bruker ATR equipped with a diamond tip in the spectral window from 4000 to 500 cm^{-1}. Unless otherwise noted, uncorrected melting points were determined in a Fisher-Johns melting point apparatus. Optical microscopy images were acquired using an Olympus BX43 microscope in a 4× zoom lens with a Samsung SM-A525 M (F1.8, 0.0 eV, 1/60, 24 mm, and ISO from 80 to 2000). In contrast, Hot-stage microscopy images were captured using a hot-stage Linkam LTS420E with a ramp program of 100 °C min^{-1}. Photoluminescence spectra and Fluorescence quantum yields (PLQY) in the solid state were measured on an Edimburg Instruments FS5 spectrofluorometer equipped with an integrating sphere (SC-30) at room temperature. Fluorescence lifetimes were measured at room temperature using the standard time-correlated single-photon counting (TCSPC) technique using a picosecond pulsed laser diode (EPL-405) at 405 nm from Edinburgh Instruments (EPL-405). Large single crystals were grown according to the procedures described below to obtain pristine powdered samples of the cocrystals. Then, the obtained crystals were slightly crushed to obtain smaller crystals with no preferred orientation confirmed through PXRD.

2.1. Synthesis of cocrystal AC-TFTA

21 mg of AC (0.06 mmol, 1 eq.) and 14 mg of TFTA (0.06 mmol, 1 eq.) were placed in a 10 mL vial. Afterward, 5 mL of dichloromethane/methanol (4 : 1) was poured into the vial, resulting in a red solution. The system was sealed and heated at 70 °C until no solids were observed. If solid matter would remain, the solution was filtered through a Pasteur pipette plugged with a small piece of cotton into another 10 mL dry vial. The cap is loosened, and the solution evaporates for 4 to 5 days to obtain yellow prismatic-shaped single crystals. They were washed with a small amount of cold methanol to dry the crystals and vacuum-filtered using a Hirsh funnel. Yield: 24 mg (85%). Elemental analysis for **AC-TFTA** ($C_{33}H_{18}F_4N_2O_4$): calc. C: 75.16, H: 3.70, N: 6.04; found C: 75.11, H: 4.04, N: 6.41.

2.2. Synthesis of cocrystal AC-PFBA

34 mg of AC (0.10 mmol, 1 eq.) and 21 mg of PFBA (0.10 mmol, 1 eq.) were placed in a 20 mL vial. Afterward, 10 mL of dichloromethane/hexane (4 : 1) was poured into the vial, forming a red solution. The heating and cooling process is the same as employed for **AC-PFBA**. The solution is allowed to evaporate for three days to obtain yellow needle-shaped single crystals. They were washed with a small amount of cold hexane to dry the crystals and vacuum-filtered using a Hirsh funnel. Yield: 45 mg (81%). Elemental analysis for **AC-PFBA** ($C_{32}H_{17}F_5N_2O_2$): calc. C: 69.07, H: 3.08, N: 5.03; found C: 68.12, H: 3.26, N: 5.29.

2.3. Cocrystal grinding

Mechanical grinding of cocrystals was performed in a planetary ball miller Fritsch® *Pulverisette 7*. Two grinding bowls of zirconium oxide (20 mL) with steel casing and sealing silicone rings were employed simultaneously, each with 160 mg of cocrystal (**AC-TFTA** or **AC-PFBA**). Additionally, each container was charged with 5 zirconium-oxide grinding balls (diameter 10 mm). The process was carried out using the neat-grinding method for 60 minutes at 850 rpm.

3. Results and discussion

3.1. Synthesis of cocrystals and SC XRD structural determination

The carbazole-acridine fused molecule, 9-(9*H*-carbazol-9-yl)-acridine, abbreviated 'AC,' consisting of an Ullmann-type coupling using Cu(I) as catalyst (Scheme S1, ESI†) was previously reported by Zeghada[42] and reproduced for this work. The title compound was characterized through ^{1}H and ^{13}C solution NMR spectroscopy (Fig. S1 and S2, ESI†), high-resolution mass spectrometry, and Fourier-transformed infrared spectroscopy, with excellent agreement with the mentioned reference. During the purification steps, we realized that saturated methanol/THF and toluene mixtures could produce yellow, prismatic-shaped crystals as solvated forms. Also, an acetonitrile solution produced the solvent-free form, as reported by Koshima.[43] Through all these structures, a twisted structure with a pronounced dihedral angle between the carbazole and the acridine fragment was visualized, likely resulting from the steric hindrance of the protons of positions 1 and 8.

The combination of AC and tetrafluoroterephthalic (TFTA) or perfluorobenzoic (PFBA) acids led to the formation of cocrystals **AC-TFTA** and **AC-PFBA** as pristine solids, which were obtained from saturated mixtures of dichloromethane/methanol and dichloromethane/hexane, respectively, suitable to be studied using single crystal X-ray diffraction (SC XRD). The collection

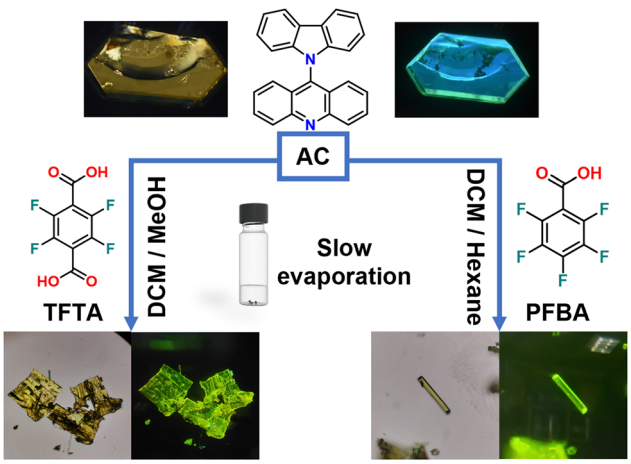

Fig. 1 Combination of AC with coformers TFTA or PFBA to form new hydrogen-bonded cocrystals. The resulting single crystals are shown under natural light and under UV light.

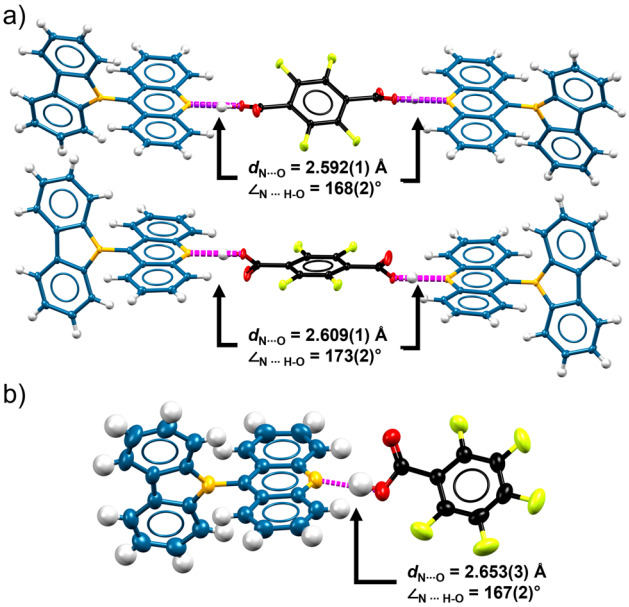

Fig. 2 Structures of (a) **AC-TFTA** and (b) **AC-PFBA**, determined through single crystal X-ray diffraction, with their respective representative hydrogen bond parameters (distances and angles). Ellipsoids are shown at 50% level probability.

and solution of the structures allowed us to elucidate a triclinic $P\bar{1}$ space group for **AC-TFTA**, while a monoclinic system $P2_1/c$ space group was determined for **AC-PFBA**. The colors and habits of their structures can be visualized in Fig. 1.

The asymmetric unit of **AC-TFTA** comprises two molecules of AC and one molecule of TFTA. However, the two molecules of AC and two complete molecules of TFTA are non-equivalent. Due to this feature, one of the TFTA molecules establishes two hydrogen bond interactions, described by a distance ($O_{donor}\cdots N_{acceptor}$) of 2.592(1) Å, while the angle $\angle N_{AC}\cdots H\text{–}O_{TFTA}$ was 168(2)°. Different parameters were observed for the other TFTA molecule, consisting of a 2.609(1) Å distance and an angle of 173(2)°. All these interactions have been represented in Fig. 2a. Regarding **AC-PFBA** (Fig. 2b), this cocrystal comprises one molecule of both donor and acceptor of hydrogen bonds in the asymmetric unit. The associated parameters for this interaction are composed of a distance of 2.653(3) Å and an $\angle N_{AC}\cdots H\text{-}O_{PFBA}$ angle of 167(2)°.

3.2. Spectroscopic features of pristine solids

The association of the corresponding carboxylic acids with the AC molecules could be visualized and further analyzed using Fourier-transform infrared spectroscopy (FTIR). Both cases illustrated in Fig. S3 (ESI†) emphasize the presence of the O–H stretching band of starting materials, which typically appears in the region between 3000–2500 cm^{-1} with a notable broadening due to the formation of dimers between the carboxylic acid molecules.[44] Contrastingly, when the cocrystallization occurs, the O–H stretching is resolved and shifted towards higher frequencies as barely perceivable bands with respect to the sole carboxylic acids. An equally visible change between the

spectra is the decrease in the intensity and position of the C=O stretching of the carbonyl towards higher frequencies when the cocrystals are formed, from 1698 to 1720 cm^{-1} for the TFTA, and from 1711 to 1714 cm^{-1} for the PFBA.[45]

The presence of a hydrogen-bond donor in the cocrystals led to interesting crystalline packings and very different photoluminescence (PL) properties compared to the starting emissive material AC, as seen in photographs from Fig. 1. Fresh samples of pristine powders were prepared to assess and compare this property. The experimental diffractograms of these solids were obtained using powder X-ray diffraction and compared against the calculated powder diffractograms from the crystallographic information files to ensure the correct phase was obtained. These are depicted in Fig. S4 (ESI†).

Next, room-temperature fluorescence spectroscopy was employed to characterize the resulting solids' photoluminescence. The PL spectra of both AC and pristine cocrystals are depicted in Fig. 3a, illustrating an emission maximum at 507 nm for the starting material AC. As for the cocrystals, their PL spectra display two emission maxima at 550 and 563 nm, corresponding to **AC-PFBA** and **AC-TFTA**, respectively. Despite the closeness in the emission wavelength of the new solids, the measured photoluminescence quantum yields (PLQY, Φ_F) are very different. At a λ_{ex} of 405 nm, the pristine AC showed a Φ_F of 74.2%, while the value for **AC-PFBA** was 26.4% and 15.4% for **AC-TFTA**.

Moreover, the time-resolved fluorescence decay experiments at room temperature allowed us to determine the lifetimes (τ) of the pristine samples. Firstly, an exponential fit with three fluorescence lifetimes was proposed for the pristine AC as a solvent-free crystalline powder (Fig. 3b). These times were 9.7 ns for τ_1, 28.3 ns for τ_2, and 48.8 ns for τ_3. These values are slightly higher for a small fluorophore in comparison with other solid-state carbazole derivatives;[46,47] which could be attributed to the rigidity of the crystal as well as lack of vibrations, owing to the π-conjugated system and strong intermolecular interactions between AC molecules.[29] On the other side, the fluorescence lifetimes of the pristine cocrystals were determined through a biexponential fit. For **AC-TFTA**, the τ_1 and τ_2 values were 7.1 and 20.3 ns, respectively, whereas for **AC-PFBA**, these were 8.3 and 21.6.

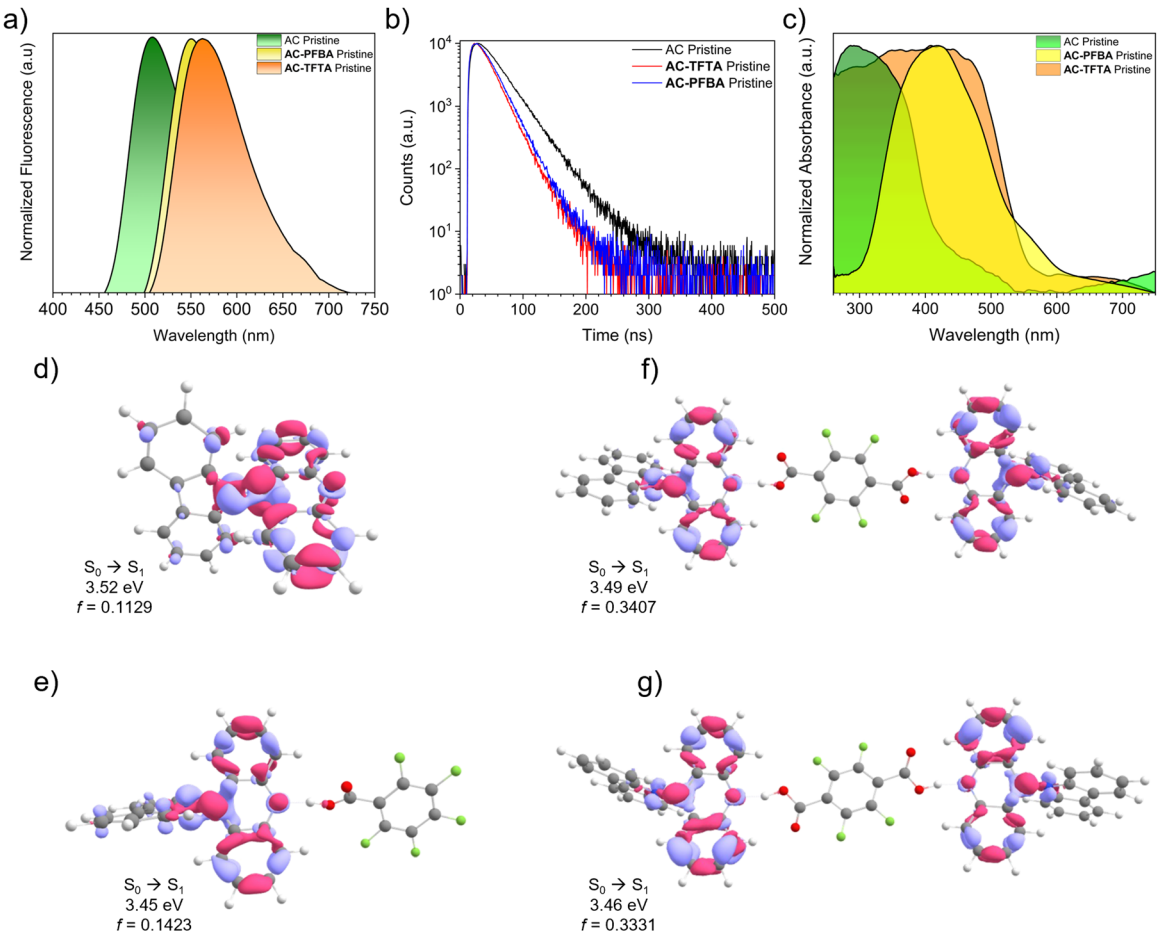

Fig. 3 Solid-state characterization of polycrystalline solids. Photophysical measurements in powdered samples: (a) room temperature photoluminescence of starting material AC and both cocrystals in their pristine forms; (b) time-resolved fluorescence decay profiles of starting material and cocrystals in the solid state at room temperature (λ_{ex} = 405 nm); (c) room temperature, solid-state absorption spectra of the compounds. Characterization of the S_1 state of (d) AC, (e) **AC-PFBA**, (f) **AC-TFTA**-a and (g) **AC-TFTA**-b at S_1 minimum. Electron density difference plots (pink positive, blue negative) for the $S_0 \rightarrow S_1$ transition computed at TD-CAM-B3LYP-D3/6-311++G(d,p) theory. Isosurface contour value = 0.02 for (d) and (e) and 0.01 for (f) and (g).

Table 1 Relevant photoluminescence parameters for the different powdered samples are presented in this work

Sample	Treatment	λ_{em} (nm)	Φ_F[a] (%)	τ_n (n = 1,2,3...) (ns)		
AC	Pristine	507	74.2	9.7	28.3	48.8
AC-TFTA	Pristine	563	15.4	7.1	20.3	
	Ground	656	0.6	5.6	15.1	32.5
	Fumed	595	2.1	6.1	15.9	31.4
AC-PFBA	Pristine	550	26.4	8.3	21.6	
	Ground	567	5.6	6.6	18.4	44.3
	Fumed	553	22.5	8.9	19.8	47.9

[a] λ_{ex} = 405 nm.

The reduction in the fluorescence lifetimes and PLQY of the cocrystals compared to AC could be attributed to the vibrational relaxation of the proton at the carboxylic acid, reducing the fluorescence in the cocrystals.[48] Another detrimental factor for fluorescence emission is the presence of π-stacking in both cocrystals, depicted in Fig. S5 (ESI†), since associated energy transfer, non-radiative processes can be involved due to orbital overlap between fragments.[49] For comparison purposes, the relevant PL data is displayed in Table 1.

To generate a deeper understanding of the photophysics of the generated solids, UV-Vis spectroscopy experiments using the diffuse reflectance technique were carried out on polycrystalline samples. From the spectra shown in Fig. 3c, a red shift in the absorption bands of the cocrystals is visualized compared to the AC powder. AC displays its maximum at *ca.* 292 nm, whereas **AC-TFTA** depicts an absorption maximum at 424 nm, and **AC-PFBA** does it at 419 nm. Moreover, through the conversion of diffuse reflectance data into Tauc plots, it was determined the optical gaps in the cocrystals, which correspond to the energy of the lowest electronic transition accessible *via* absorption of a single photon.[50] For the case of **AC-TFTA**, this energy corresponds to 2.32 eV; for **AC-PFBA**, it is 2.36 eV. The comparative plot can be visualized in Fig. S6 (ESI†).

3.3. Theoretical calculations based on the SC-XRD structures of cocrystals

We investigated the electronic transitions behind the absorption and emission spectra in the crystalline phase for pure AC crystal and both cocrystals. First, the crystals were refined using periodic DFT (see Computational details in the ESI†). Then, we considered embedded quantum mechanics (QM: QM′) cluster models implemented in the *fromage* package to analyze the excited states.[51,52] Considering a molecular-centered mechanism, as previously done for similar carbazole-based crystalline systems[53,54] the QM region was defined to be a monomer (AC), dyad (**AC-PFBA**), or triad (**AC-TFTA**) and was described as the TD-CAM-B3LYP-D3/6-311++G(d,p) level of theory. The QM' region consists of a semi-spherical radius cluster ∼22 Å and was described by the GFN2 extended tight binding (GFN2-xTB) Hamiltonian. Further details are provided in the ESI.†

The S_1 of AC is a transition mainly located over the acridine moiety (Fig. 3d) with absorption at 352 nm (3.52 eV), slightly red-shifted to the experimental maximum absorption peak at 292 nm. Upon cocrystallization, the S_1 state of the dyad and triads remains with the same local excitation character over the AC molecule. The energy of the $S_0 \rightarrow S_1$ transition is 3.45 eV for **AC-PFBA** with an oscillator strength of 0.1423, which is very close to the computed values for the AC crystal (Fig. 3e). In the case of the asymmetric triads observed in the **AC-TFTA**, S_1, and S_2 are quasi-degenerated, resulting from the in-phase (out-phase) electronic transition dipole moment interaction of the $S_0 \rightarrow S_1$ transition of each AC fragment.[55] While S_1 (Fig. 3f and g) is the brighter state, whose *f* is around twice the value computed for AC and **AC-PFBA**, the S_2 of **AC-TFTA**-a(b) is a dark state with excitation energy of 3.50 eV (3.47 eV). Due to the degree of localization of the orbitals, the energies of the frontier orbitals of the cocrystals are closer to the ones of the pure AC crystal, as can be observed in Fig. S7 (ESI†).

To simulate the photoluminescence properties of the cocrystals, we obtained the optimized geometry for the S_1 state using the same ONIOM QM: QM′ embedded scheme described before. The predicted emission energy of the pristine AC crystal is 2.99 eV, which overestimates the experimental maximum (507 nm, 2.45 eV) by around 0.5 eV. The predicted values for **AC-PFBA** and **AC-TFTA** are slightly red-shifted (around 0.1 eV) for both crystals, which agrees with the experimental results for both the absorption maxima and the optical gaps. In both cocrystals, the PL originated from the S_{1min} geometry, localized on the AC molecule with almost no influence of the acid. This explains the very close emission of **AC-PFBA** and **AC-TFTA** with AC. The generation of orbitals and associated energies are visualized in Fig. S8 (ESI†).

3.4. Decarboxylation-mediated thermosalient effect of AC-TFTA

As we described in the introduction of this work, TFTA and PFBA are coformers used in the synthesis of cocrystals with photosalient and thermosalient effects. Driven by these precedents, we decided to test the capabilities of our cocrystals toward thermal responsiveness. Regarding **AC-TFTA**, it was observed that when single crystals of this solid (as a pristine sample) were heated using a Fisher-Johns apparatus, these started to jump out of the plate at *ca.* 265 °C, as visualized in the progressive images from Fig. S9 and Movie S1 (ESI†).

To gather more detailed information on the macroscopic phenomena, we used Hot-Stage microscopy with a heating ramp setup of 100 °C min^{-1}, coupled with a high-speed camera. The resulting cut frames from the original movie (Movie S2, ESI†) display that when the temperature approaches 260 °C, the material starts to lose some crystallinity, as seen from the darkening of the prisms under polarized light. Afterward, a swift collapse of the crystals occurs in a direction towards the center of the prisms along the significant diagonal, as described in the arrows of Fig. 4a.

Surprised by our observations, a fresh sample of pristine **AC-TFTA** was studied through coupled differential scanning calorimetry and thermogravimetric analyses (DSC/TGA). It was observed that the DSC curve highlights an endothermal peak from 245 up to 270 °C, with a maximum of 262 °C (Fig. 4b).

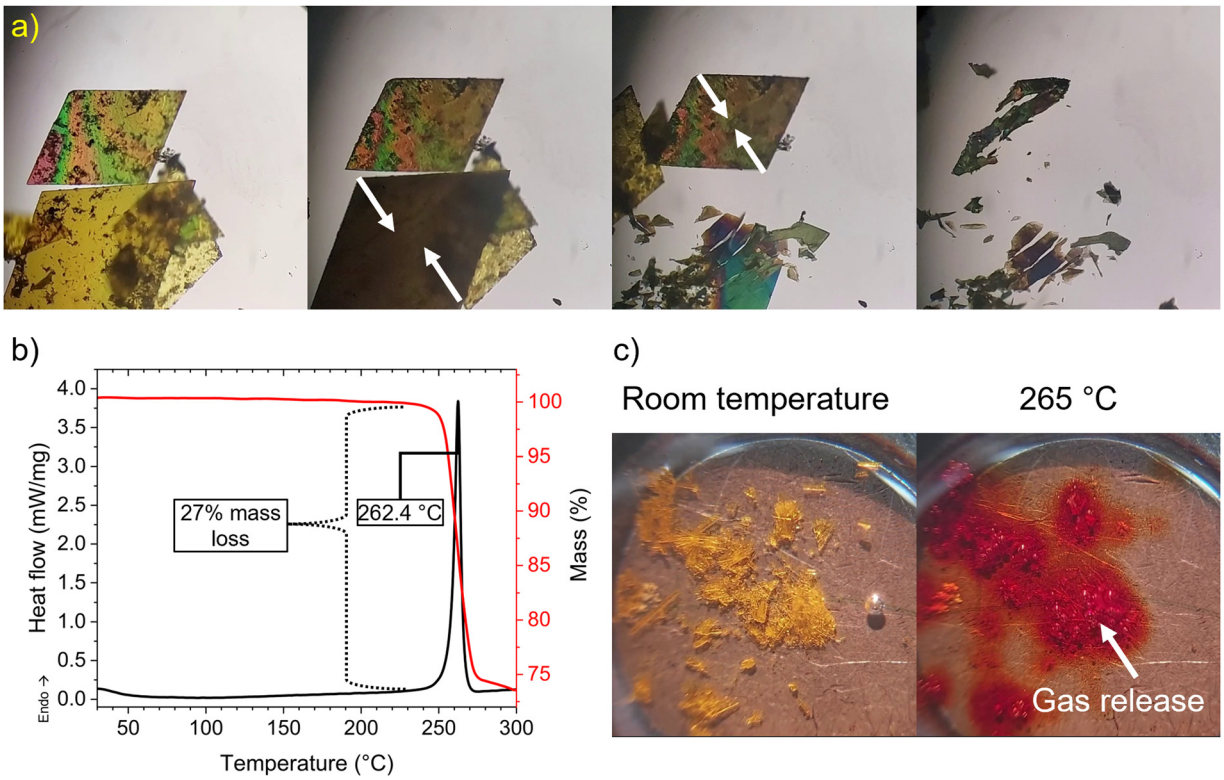

Fig. 4 (a) Hot-stage microscopy frames showing the detail on the thermosalient effect of **AC-TFTA** single crystals due to the decarboxylation of TFTA. The images were captured with a high-speed camera and display the process of loss of crystallinity (darkening) of the prisms and compression along the major axis of the prismatic material; (b) DSC/TGA curves of pristine **AC-TFTA** displaying the percentage loss of mass and the endothermal associated with the thermosalient effect; (c) photographs of single crystals of **AC-TFTA** on a hot-plate, layered in Parabar to observe the release of CO_2 gas due to the heating.

Interestingly, the interval of temperatures matches with a 27% loss of mass from the initial sample from the TGA curve, which could be initially associated with the loss of CO_2 molecules.

To confirm the identity of the molecules released during the heating process, freshly grown single crystals of **AC-TFTA**, covered by a thin layer of Parabar 10312 (an oil used for crystallographic purposes), were placed on the Fisher-Johns melting apparatus. Towards 260 °C, it was observed that a large amount of bubbles emanated from the oil, followed by the melting of the remaining material (Fig. 4c). This process was recorded in Movie S3 (ESI†). Subsequently, we relied on the characterization of the volatile compounds through gas chromatography (GC) coupled to mass spectrometry. A sealed vial, with an initial quantity of the pristine **AC-TFTA**, was loaded and purged with N_2, then heated towards 270 °C, and the volatile compounds generated were injected into the GC. The resulting chromatogram is shown in Fig. S10a (ESI†), which displays the resolution of several peaks. The detection of each peak and its associated compound is depicted in the spectrograms of Fig. S10b–h (ESI†). A series of fragmentations of the AC and the TFTA molecules could be identified, especially carbon dioxide and tetrafluorobenzene, due to the decomposition of TFTA. At longer retention times, the presence of acridine, carbazole, and AC molecules was also detected.

After submitting a sample of **AC-TFTA** under complete decarboxylation, we gathered information on the identity of the remaining solid. The residual yellow powder after the heating process was characterized using PXRD and fluorescence spectroscopy in the solid state. From Fig. S11a (ESI†), the PXRD diffractogram shows a series of broad reflections that barely agree with any of the diffractograms for AC pristine or **AC-TFTA**. On the other hand, Fig. S11b (ESI†) displays the PL spectra of the compound with an emission maximum of 468 nm for the recovered solid. The DSC/TGA curve of pristine AC is shown in Fig. S12 (ESI†), which displays the melting of the sole compound at 255 °C. The data shows that a new crystalline phase of residual AC is present after the dramatic heating of the cocrystals towards the thermosalient effect and further cooling at room temperature.

Overall, the joint evidence led us to postulate that a decarboxylation of the TFTA coformer inside the crystalline network was responsible for the thermosalient effect, followed closely by the melting of AC. Contrastingly, we did not observe the decarboxylation effect on crystalline TFTA on its own. To corroborate this, crystals of TFTA were studied through DSC/TGA (Fig. S13, ESI†). The curves display the sublimation of TFTA starting from 250 °C up to an endothermal peak at 283 °C.

Similar tests were carried out for the single crystals of **AC-PFBA**. The heating of freshly grown samples in the melting apparatus did not show the described jumping behavior. A recording of the visual changes under UV light (254 nm) through the heating interval can be recovered from Movie S4

(ESI†). Furthermore, crystals of **AC-PFBA** were placed, covered with Parabar, and heated up to 260 °C. In Movie S5 (ESI†), a slow release of bubbles was observed, starting at *ca.* 180 °C and continuing up to 230 °C. More information was obtained through the DSC/TGA curves of pristine **AC-PFBA** (Fig. S14, ESI†), which show an endothermal peak at 177 °C, in agreement with a mass loss of 37.5%, corresponding to the release of complete PFBA molecules, instead of a decarboxylation process. As the temperature increases, the DSC profile shows a new endotherm at 267 °C, which can be associated with the melting of AC.

The significantly different thermal responses in both samples led us to find a feasible explanation through the analysis of their non-covalent energy interactions for each crystalline packing. For this matter, we performed theoretical calculations using the CE-B3LYP[56] 6-31G(d,p) functional implemented in CrystalExplorer 21.5.[57] The resulting energy values suggest that the hydrogen bond interactions in **AC-TFTA** (*ca.* −58 to −61 kJ mol^{-1}) are stronger than in **AC-PFBA** (*ca.* −53 kJ mol^{-1}). Both values are in agreement with some reports of the association of carboxylic acids and acridines through hydrogen bonds in the solid state.[58–61]

Despite this fact, the distribution of weaker non-covalent interactions, such as C–H···π, is somewhat different in both cocrystals. For instance, it was observed that the non-covalent interactions around the TFTA molecules in **AC-TFTA** range from −7 to −9 kJ mol^{-1}. In sharp contrast, inside **AC-PFBA**, the non-covalent interactions of the PFBA molecules with neighboring molecules are stronger and range between −15 to −29 kJ mol^{-1} for adjacent PFBA molecules and −32 kJ mol^{-1} for AC fragments.

The contrasting energy differences between both cocrystals indicate a higher anisotropy in the crystalline packing of **AC-TFTA** against the more uniform **AC-PFBA** moiety. As described recently by Geerts and coworkers, the anisotropy derived from different non-covalent interactions can result in dramatic effects in the mechanical and responsive properties of crystals, also providing a methodology for the slow or fast release of organic molecules or gases with thermosalient effects.[38] For illustration purposes, Fig. 5a and b highlights the strongest interactions around fluorinated molecules in each cocrystal. To complement the analyses, Hirsfeld surfaces of the fragments are depicted as insets in the corresponding fingerprint plots (Fig. S15 and S16, ESI†), where the principal interactions of these cocrystals are displayed.

3.5. Mechanical induction of photophysical and structural changes in cocrystals

The presence of different degrees of anisotropy in the cocrystals herein described motivated us to explore changes in the photophysical properties of the pristine solids *via* mechanical stress through the grinding of microcrystalline samples. For this purpose, a planetary ball-miller was employed, as described in the Experimental section. After one hour of grinding at 850 rpm, the two solids featured abrupt changes in their physical appearances. Fig. 6a depicts a visual comparison of the powders before and after the grinding. **AC-TFTA** displayed a deep-red color upon grinding, whereas **AC-PFBA** resulted in a faint orange color.

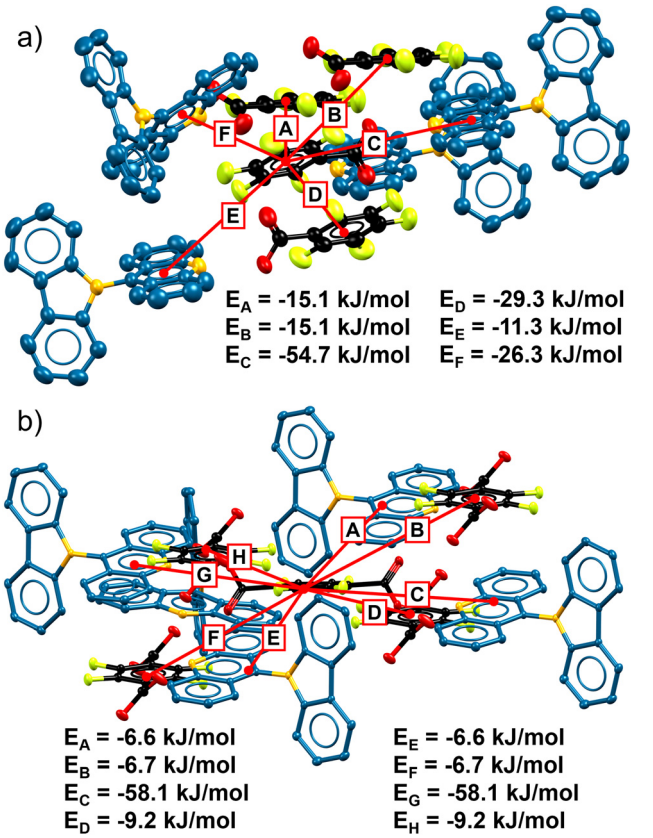

Fig. 5 Distribution of non-covalent interaction energies in (a) **AC-PFBA** and (b) **AC-TFTA**, obtained from calculations at the *CE*-B3LYP 6-31G(d,p) level of theory in CrystalExplorer 21.5.

The characterization of the crystallinity, performed through PXRD at room temperature, showed remarkable differences between both powders. Firstly, the ground powder of **AC-TFTA** is significantly amorphized compared to ground **AC-PFBA** under the same conditions, as shown in Fig. S17 (ESI†). A LeBail analysis of the experimental diffractograms helped us determine the percentage of crystalline material remaining after the milling of the solids. While **AC-TFTA** displayed a 20% of crystalline material remaining, **AC-PFBA** contained 52% of crystalline powder under the same grinding conditions.

To quantitatively compare the absorption of the new powders due to the grinding, Fig. 6b portrays the UV-Vis profiles of both cocrystals after the grinding process. It can be visualized that **AC-TFTA**, after grinding, displays a significantly broader band, extended up to *ca.* 600 nm, with an absorption maximum of 365 nm. On the other hand, the broadening of the absorption in **AC-PFBA** is not as dramatic as in the previous cocrystal, extended towards 520 nm. Similarly to the pristine solids, the data from diffuse reflectance was employed in calculating the energy optical gaps, through the Tauc plots displayed in Fig. S18 (ESI†). The obtained values were considerably lower than those for pristine solids, being 2.02 eV for **AC-TFTA** against 2.22 eV for **AC-PFBA.**

Regarding the PL of the ground solids, the spectra are shown in Fig. 6c. It highlights an emission maximum of 656 nm for

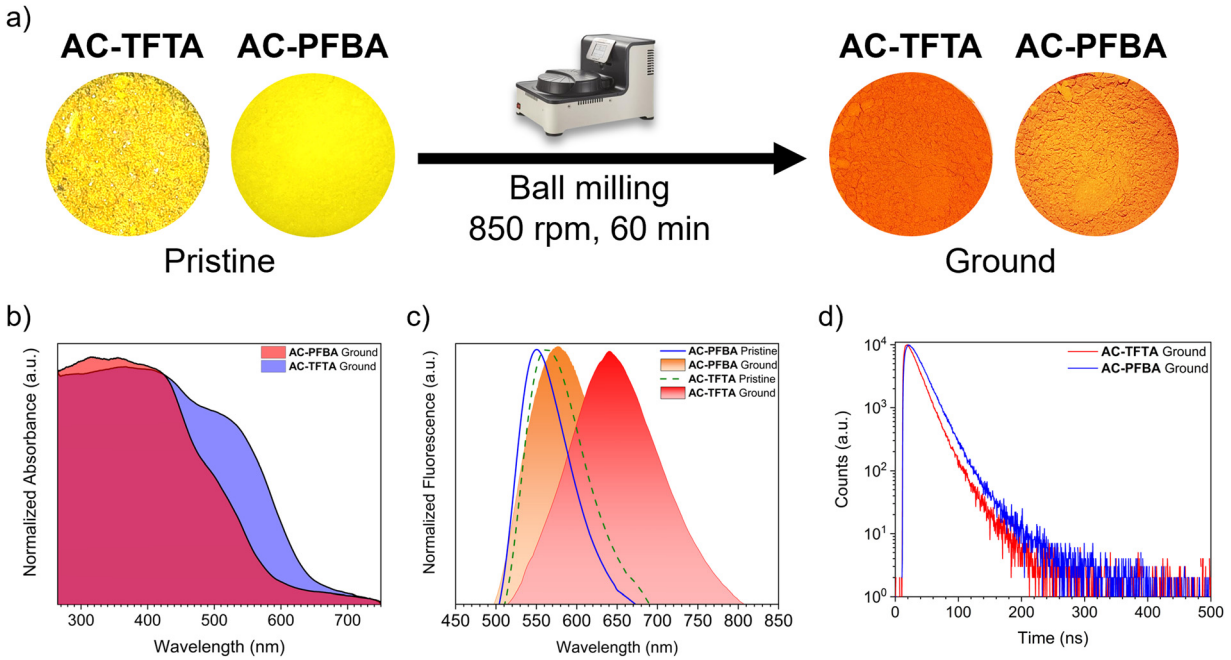

Fig. 6 Schematics of induction of mechanical stress on crystalline samples of cocrystals herein reported: (a) appearance of the solids of **AC-TFTA** and **AC-PFBA** as pristine and ground samples. Pictures were obtained under natural light. Solid-State spectroscopic characterization of the resulting powders through (b) absorption and (c) fluorescence spectroscopies. For comparison purposes, the PL spectra of pristine solids are shown in panel c, against the obtained for grounds samples. (d) Solid-state, room temperature time-resolved fluorescence decay profile of ground powders (λ_{ex} = 405 nm).

AC-TFTA, while for **AC-PFBA**, it is 567 nm. In comparison with the pristine samples, **AC-TFTA** showed a bathochromic shift of 93 nm, and **AC-PFBA** only showed a 17 nm red-shift. The ground samples showed a dramatic quenching in the fluorescence; in the case of **AC-TFTA**, the PLQY went from 15.4% to 0.6%, and for **AC-PFBA**, the value changed from 26.4% to 5.6%. The smaller values of quantum yields agree well with a higher contribution of amorphous solid component, with a rise in the degree of freedom of the molecules, promoting more effective vibrational relaxations.[62] Additionally, the time-resolved fluorescence decay profiles were determined for these samples (Fig. 6d). The concentrated data is displayed in Table 1, which shows that for both **AC-TFTA** and **AC-PFBA**, the decay was fitted as a three-component exponential.

3.6. ssNMR experiments of pristine and ground powders

To provide a deeper understanding of the structural changes of the transformation from grinding, we used solid-state nuclear magnetic resonance (ssNMR) through the cross-polarization (CP) magic-angle spinning (MAS) for ^{13}C and direct pulse with MAS for ^{19}F. Fig. 7a shows that for the case of crystalline **AC-TFTA**, a ^{13}C CP MAS spectrum with six signals between 100 and 165 ppm is presented. When this spectrum is compared with the ground powder, a broadening of signals is evident, especially with the pair of signals centered at 123 and 119 ppm. This effect is attributed to the different orientations of the ^{13}C carbon atoms due to the amorphization of the sample. A less pronounced broadening is observed for the signals in the **AC-PFBA** spectra from Fig. 7b.

Even more interestingly, significant changes are observed in the ssNMR ^{19}F MAS spectra of both cocrystals. The comparison of ground and pristine **AC-TFTA** at room temperature is shown in Fig. 7c. A set of signals between −130 and −145 ppm correspond to the fluorine atoms of the TFTA when the periodic arrangement is intact. On the other hand, upon amorphization of the sample, the resolution of the signals is notoriously

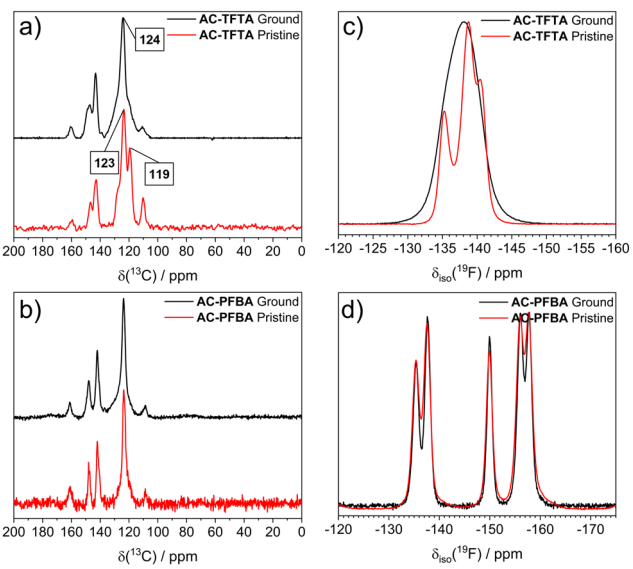

Fig. 7 Characterization of pristine and ground powders of cocrystals through ssNMR. ^{13}C MAS spectra with cross-polarization (125.8 MHz, Spin Rate = 20 kHz, d_1 = 20 s) of (a) **AC-TFTA**, and (b) **AC-PFBA** ^{19}F MAS spectra (470.6 MHz, Spin Rate = 20 kHz, d_1 = 10 s) of (c) **AC-TFTA**, and (d) **AC-PFBA**. In these spectra, only the central signals are shown. For the full spectra, please visualize the ESI† file.

diminished, resulting in the coalescence into a broadened signal centered at −143 ppm. Additional experiments at variable temperatures (Fig. S19, ESI†) were conducted to evaluate possible changes in the chemical shift of the signals. However, no noticeable effects were observed through the temperature interval between 248 and 308 K. For the case of **AC-PFBA**, even after the thorough grinding process, the ^{19}F spectra associated with both pristine and ground solids remain essentially unaltered both at room (Fig. 7d) and low temperatures (248 K), as can be seen from Fig. S20 (ESI†).

3.7. Regeneration of crystallinity through thermal and fuming stimuli

A practical yet not fully understood feature of mechanofluorochromic materials is their capability to regenerate their crystalline structure through the application of external stimuli, such as solvent vapors or temperature. We were curious to unveil whether these cocrystals portrayed this type of behavior. For this matter, we placed a portion of each ground powder in a holder and then immersed it in a beaker previously saturated with dichloromethane vapors. After 10 minutes of fuming for both powders, there was a noticeable change in the colors, with **AC-TFTA** the most notable return from the red coloration to a faint yellow. In contrast, the faint orange of **AC-PFBA** was quickly returned to its original yellow.

The color changes were recorded and can be visualized in Movie S6 (ESI†). The vapor-treated powders were characterized through PXRD to examine the degree of crystallinity after the whole process. The resulting data, presented in Fig. 8a and b, allowed us to visualize the regeneration of the crystalline solid with good agreement between the reflections of the experimental diffractogram and the calculated from SC XRD structures. Moreover, the photophysical parameters for these solids were determined. The Fig. S21 (ESI†) displays the solid-state fluorescence spectra of the fumed solids, depicting a λ_{em} of 595 nm for **AC-TFTA**, different from the 563 nm determined for the pristine sample. Meanwhile, for **AC-PFBA**, the maximum appears at 553 nm, which is extremely close to the initial 550 nm of the pristine sample.

Furthermore, the quantum yields of the fumed samples were measured. It was clear that for **AC-TFTA**, not only was the emission maximum drastically changed, but it also suffered a quenching in the emission of the powder with a 2.1% yield. The determined fluorescence lifetimes of this fumed sample were 6.1, 15.9, and 31.4 ns, which closely resemble the lifetimes of the ground powder. Contrastingly, the fumed powder of **AC-PFBA** showed a remarkable 22.5% yield against the 26.4% of the pristine sample, while the fitted fluorescence lifetimes were determined to be 8.9, 19.8, and 47.9 ns. The decay curves are shown in Fig. 8c.

Due to the contrasting results in the recovery, we decided to perform fatigue tests on powdered samples of both cocrystals. For this purpose, three grinding-recovery (fuming) cycles were carried out. Fluorescence spectroscopy was employed to monitor the regeneration of the crystalline phase. The reduced spectral data is displayed in Fig. 8d, and the progressive solid-state spectra are depicted in Fig. S22 and S23 (ESI†). From the fuming of **AC-TFTA** in the first cycle, this powder showed clear signs of fatigue, as seen in the ever-smaller differences between the emission wavelength of the ground and the fumed sample. By the end of the third cycle, the difference between emission maxima was only 21 nm (from 600 to 579 nm), in contrast to the first grinding-fuming with a difference of 61 nm. On the other side, **AC-PFBA** showed remarkable recovery properties under fuming since the most significant difference between the ground and the fumed samples was only 21 nm and occurred during the second cycle.

Afterward, we tested the thermal-induced regenerating capabilities of the ground powders. First, we decided to gather information on the thermal stability and behavior of ground powders. The resulting calorimetric and thermogravimetric analysis can be visualized in Fig. 9a. **AC-TFTA**, in its ground form, showed notable changes in the DSC curve in comparison with the pristine solid. From 78 °C and up to 245 °C, the DSC displays a progressive, increasing heat flow, which can be associated with the gradual migration of the amorphous solid to regenerate the crystalline arrangement. Afterward, an exotherm at 252 °C, which is aligned with a mass loss of 22% (from the TGA curve), could be related to the progressive decomposition of TFTA, expelling CO_2. Finally, an endothermal peak towards 267 °C features the melting of AC coformer.

A similar case is exposed for **AC-PFBA** ground, which displays a slow but continuous heat entry until an endotherm at 166 °C is evident, in agreement with the expulsion of PFBA and a 35% loss of starting mass. Afterward, at *ca.* 266 °C, as happened in **AC-TFTA**, an endotherm is presented, which could also be associated with the melting of AC.

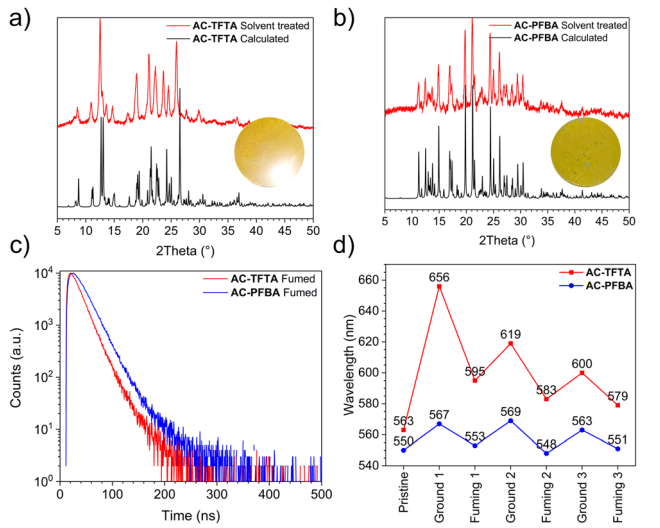

Fig. 8 PXRD diffractograms of fumed samples compared against calculated PXRD form SC XRD for (a) **AC-TFTA** and (b) **AC-PFBA**. The appearance of the fumed solids is shown as insets in each diffractogram under natural light; (c) time-resolved fluorescence decay of the fumed samples and (d) relevant data from fatigue tests performed on the cocrystals. The regeneration of samples was carried out through the fuming of samples with DCM vapours.

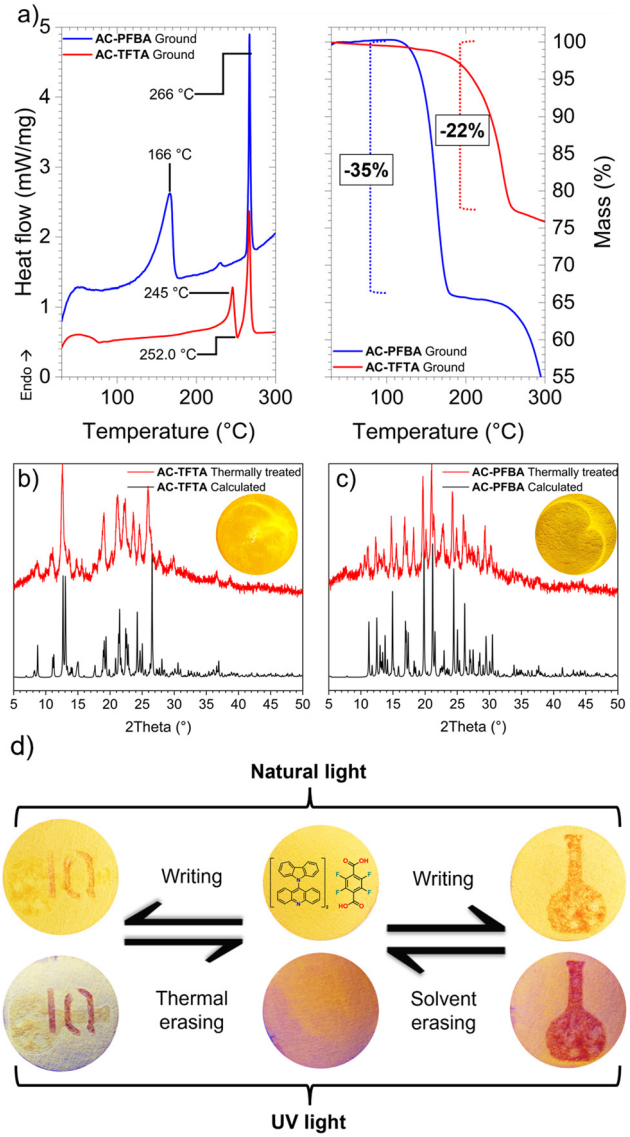

Fig. 9 (a) DSC/TGA curves of ground powders; (b) and (c) PXRD profile of thermally treated powders of the cocrystals herein reported. As inset in each PXRD a picture shows the appearance of the powder after 10 minutes of heating on a hot plate at 80 °C under natural light; (d) drawing-erasing cycles with heat and DCM vapours of a filter paper with dispersion of **AC-TFTA** powders on the surface.

To obtain visual evidence of the recovery of crystallinity under thermal stimuli, amounts of both ground cocrystals were placed on a glass holder and put on a hot plate at 80 °C for 10 minutes. The transition was recorded in Movie S7 (ESI†), and the characterization of the thermal-treated powders was carried out through PXRD. The diffractograms are exposed in Fig. 9b and c, with insets of the appearance of the resulting solids after the thermal treatment. Despite the recovery of some of the initial crystallinity, especially in **AC-TFTA**, it is notorious that the crystalline phase is not fully recovered under the conditions employed, with the presence of a higher amorphous component in comparison with the PXRD obtained for the fuming procedure.

The regeneration of the crystalline phases due to external stimuli is an ongoing field of study. So far, the evidence collected not only in this manuscript but also in previous works suggests that the presence of highly twisted, rigid fragments plays a role in the change in the photophysical properties during the grinding process, overall, changing the dihedral angles between fragments, modifying the π-conjugation across the system, with a subsequent change in the absorption of the material, as visualized from Fig. 6.[9,46,63] A synergistic effect between the amorphization of the crystalline structure and the torsional changes of molecules give rise to a metastable phase. This phase, overall, in an amorphous state, should contain seeds of remaining microcrystals capable of inducing the regeneration of the crystalline solid when the external stimuli are applied. The degree of regeneration of these materials can vary with the anisotropy of the crystalline packing.[33] If the distribution of the non-covalent interaction energies around the molecules is similar, as in the case of **AC-PFBA** herein presented, the recovery of the material should occur with a high probability. On the contrary, if some energies are remarkably different from the rest, as in **AC-TFTA**, the regeneration of the crystalline phase will rely primarily on the recovery of these non-covalent interactions, with a lower probability of recovery and a high tendency towards fatigue.

3.8. Potential of AC-TFTA towards application in anticounterfeiting

Finally, due to the dramatic change of color upon grinding and to qualitatively show the possible use of **AC-TFTA** towards anticounterfeiting applications, a filter paper was soaked in a DCM/MeOH solution (1 : 1) containing AC and TFTA. The paper was left to slowly dry at room temperature, generating a yellow canvas in which, by applying mechanical pressure with a mortar pestle, we first drew the silhouette of a flat-bottom flask, as depicted in Fig. 9d. Then, the paper was treated in a chamber containing DCM vapors for 10 minutes. It was observed that the first figure was erased, and the initial yellow canvas was left almost intact. On the same paper, we proceeded to draw the letters '*IQ*', which stands for "Instituto de Química," then the paper was heated on a hot surface at *ca.* 80 °C for 10 minutes, which produced the same erasing effect. This experiment led us to corroborate that the regeneration of the photophysical properties of **AC-TFTA** not only occurs in the microcrystalline solid but also when it is supported on a paper surface.

4. Conclusions

In this manuscript, we have taken advantage of the cocrystallization technique through the usage of an acridine/carbazole hydrogen-bond acceptor and thoughtfully combined it with two fluorinated carboxylic acids. Despite the apparent similarities in the structures of the acids, we found very different non-covalent interactions, leading to varying behaviors of the cocrystals upon mechanical grinding. Even more interestingly, we have obtained insights into the structural and spectroscopic

features of the pristine and ground cocrystals, as well as described the regeneration processes of their crystallinity under solvent and thermal stimuli, provided feasible origins of the photoluminescence in both structures, and characterized both facets of these solids *via* solid-state NMR techniques, UV-Vis and fluorescence spectroscopy, and differential scanning calorimetry. Our results show that the cocrystal **AC-TFTA** features a more fragile crystalline packing than its analogue **AC-PFBA**, which is translated into more dramatic changes in photoluminescence, UV-Vis absorption, and thermal stability. Interestingly, one of the cocrystals showed a high-temperature jumping effect due to decarboxylation. The work herein reported provides deep insights into the development of stimuli-responsive materials with additional jumping capabilities through the release of gas as a driving force.

Data availability

The data supporting this article has been included as part of the ESI.† Further information can be provided upon reasonable request from the corresponding author. E-mail: brodriguez@iquimica.unam.mx.

Conflicts of interest

The authors declare no competing interests.

Acknowledgements

DGAPA PAPIIT IN207222 and CONAHCYT Ciencia de Frontera 1715644 financially supported this work. A. N.-H. Thanks, CONAHCYT, for a PhD scholarship (957838). Y. A. A.-S. acknowledges the support from the DGAPA-UNAM postdoctoral fellowship. We acknowledge the technical assistance from Mayra León-Santiago MSc. (GC-MS, Laboratorio Nacional de Ciencias para la Investigación y Conservación del Patrimonio Cultural, LANCIC), Dr Ma. C. García-González and Dr J. F. Pérez-Flores (MS); Dr M. E. García-Aguilera, Ma. Angeles Peña-González BSc, Dr B. Quiroz, Dr I. Chávez, E. Huerta-Salazar MSc and Dr R. Gaviño (solution NMR); Dr U. Hernández, M. Tapia MSc (PXRD); Dr A. Romo-Pérez (FTIR); Dr D. Martínez-Otero (SCXRD) and MSc. Virginia Gomez-Vidales (EPR). We thank Dr P. Guadarrama, Dr Diego Solis-Ibarra and N.C. Cabrera-Quiñones MSc for instrumentation access. We are also thankful for computer time LANCAD-UNAM-DGTIC-392. R. C. O. and M. E. S. S. acknowledge the use of the UCL High Performance Computing Facilities Myriad@UCL and Kathleen@UCL and funding by the UK Research and Innovation under the UK government's Horizon Europe funding guarantee (grant number EP/X020908/2).

Notes and references

1 F. Khan, A. Ekbote, G. Singh and R. Misra, Mechanochromic luminogens with hypsochromically shifted emission switching property: recent advances and perspectives, *J. Mater. Chem. C*, 2022, **10**, 5024–5064.
2 J. Guo, C. Hu, J. Liu, Y. Wang and L. Ma, Mechanochromism, tunable pure organic room temperature phosphorescence, single-molecule near-white emission, digital encryption, and anti-counterfeiting, *Dyes Pigm.*, 2024, **221**, 111760.
3 Y. Yin, Q. Guan, Z. Chen, D. Deng, S. Liu, Y. Sun and S. H. Liu, Force-triggered hypso- and bathochromic bidirectional fluorescence switching beyond 120 nm and its anticounterfeiting applications, *Sci. Adv.*, 2024, **10**, eadk5444.
4 W. Shi, B. Rong, S. Li, Y. Lin, Y. Liao, C. Cao, S. Pan and B. Wei, Mechanochromic properties of acridine heterocyclic derivatives with a donor-acceptor configuration, *J. Mol. Struct.*, 2024, **1308**, 138050.
5 P. Gayathri, S. Ravi, P. Nantheeswaran, M. Mariappan, S. Karthikeyan, M. Pannipara, A. G. Al-Sehemi, D. Moon and S. P. Anthony, CF3 H-bonding locked aromatic stacking of picric acid with mechanofluorochromic fluorophores: highly selective reusable sensor and rewritable fluorescence platform, *Mol. Syst. Des. Eng.*, 2022, **7**, 1277–1286.
6 P. Gayathri, P. Nantheeswaran, M. Mariappan, S. Karthikeyan, M. Pannipara, A. G. Al-Sehemi, D. Moon and S. P. Anthony, Methoxy substituent facilitated wide solvatofluorochromism, white light emission, polymorphism and stimuli-responsive fluorescence switching in donor-π-acceptor, *Spectrochim. Acta, Part A*, 2023, **286**, 121989.
7 Y. Wang, W. Liu, L. Ren and G. Ge, Deep insights into polymorphism initiated by exploring multicolor conversion materials, *Mater. Chem. Front.*, 2019, **3**, 1661–1670.
8 S. Saotome, K. Suenaga, K. Tanaka and Y. Chujo, Design for multi-step mechanochromic luminescence property by enhancement of environmental sensitivity in a solid-state emissive boron complex, *Mater. Chem. Front.*, 2020, **4**, 1781–1788.
9 M. C. García-González, A. Navarro-Huerta, F. C. Rodríguez-Muñoz, E. G. Vera-Alvízar, M. A. Vera Ramírez, J. Rodríguez-Hernández, M. Rodríguez and B. Rodríguez-Molina, The design of dihalogenated TPE monoboronate complexes as mechanofluorochromic crystals, *CrystEngComm*, 2021, **23**, 5908–5917.
10 J. Xiong, K. Wang, Z. Yao, B. Zou, J. Xu and X.-H. Bu, Multi-Stimuli-Responsive Fluorescence Switching from a Pyridine-Functionalized Tetraphenylethene AIEgen, *ACS Appl. Mater. Interfaces*, 2018, **10**, 5819–5827.
11 T. Sun, D. Cheng, Y. Chai, J. Gong, M. Sun and F. Zhao, High contrast mechanofluorochromic behavior of new tetraphenylethene-based Schiff base derivatives, *Dyes Pigm.*, 2019, **170**, 107619.
12 S. Takahashi, S. Nagai, M. Asami and S. Ito, Two types of two-step mechanochromic luminescence of phenanthroimidazolylbenzothiadiazoles, *Mater. Adv.*, 2020, **1**, 708–719.
13 R. Kubota, Y. Yuan, R. Yoshida, T. Tachikawa and S. Ito, Tunable mechanochromic luminescence *via* surface protonation of pyridyl-substituted imidazole crystals, *Mater. Adv.*, 2022, **3**, 5826–5835.
14 W. Wang, R. Li, S. Xiao, Q. Xing, X. Yan, J. Zhang, X. Zhang, H. Lan and T. Yi, Design of High-Contrast Mechanochromic

Materials Based on Aggregation-Induced Emissive Pyran Derivatives Guided by Polymorph Predictions, *CCS Chem.*, 2022, **4**, 899–909.

15 T. Seki, Y. Takamatsu and H. Ito, A Screening Approach for the Discovery of Mechanochromic Gold(I) Isocyanide Complexes with Crystal-to-Crystal Phase Transitions, *J. Am. Chem. Soc.*, 2016, **138**, 6252–6260.

16 R. Zhang, J.-W. Liu, W.-Y. Zhong, J.-L. Chen, F. Zhao, S.-J. Liu and H.-R. Wen, Mechanochromic and Selective Vapochromic Solid-State Luminescence of a Dinuclear Cuprous Complex, *Inorg. Chem.*, 2023, **62**, 11510–11517.

17 P. Yu, D. Peng, L.-H. He, J.-L. Chen, J.-Y. Wang, S.-J. Liu and H.-R. Wen, A Mechanochromic and Vapochromic Luminescent Cuprous Complex Based on a Switchable Intramolecular $\pi\cdots\pi$ Interaction, *Inorg. Chem.*, 2022, **61**, 254–264.

18 S. Cheng, Z. Chen, Y. Yin, Y. Sun and S. Liu, Progress in mechanochromic luminescence of gold(I) complexes, *Chin. Chem. Lett.*, 2021, **32**, 3718–3732.

19 C. Xing, Z. Qi, B. Zhou, D. Yan and W.-H. Fang, Solid-State Photochemical Cascade Process Boosting Smart Ultralong Room-Temperature Phosphorescence in Bismuth Halides, *Angew. Chem., Int. Ed.*, 2024, **63**, e202402634.

20 Y.-J. Ma, G. Xiao, X. Fang, T. Chen and D. Yan, Leveraging Crystalline and Amorphous States of a Metal-Organic Complex for Transformation of the Photosalient Effect and Positive-Negative Photochromism, *Angew. Chem., Int. Ed.*, 2023, **62**, e202217054.

21 D. K. Sivadas, P. Gayathri, S. Ravi, S. Karthikeyan, M. Pannipara, A. G. Al-Sehemi, D. Moon, S. P. Anthony and V. Madhu, Distinct fluorescence state, mechanofluorochromism of terpyridine conjugated fluorophores and the reusable sensing of nitroaromatics in aqueous medium, *New J. Chem.*, 2023, **47**, 12770–12778.

22 H.-W. Liang, T. Jia, X. Yong, J.-K. Yu, Y. Yi, S. Lu, L. Wang and H. Wang, Photoinduced Single-Crystal to Single-Crystal Transformation *via* Conformational Change with Turn-On Fluorescence, *Cryst. Growth Des.*, 2022, **22**, 2082–2086.

23 S. Ito, Recent Advances in Mechanochromic Luminescence of Organic Crystalline Compounds, *Chem. Lett.*, 2021, **50**, 649–660.

24 L. Sun, W. Zhu, X. Zhang, L. Li, H. Dong and W. Hu, Creating Organic Functional Materials beyond Chemical Bond Synthesis by Organic Cocrystal Engineering, *J. Am. Chem. Soc.*, 2021, **143**, 19243–19256.

25 L. Sun, Y. Wang, F. Yang, X. Zhang and W. Hu, Cocrystal Engineering: A Collaborative Strategy toward Functional Materials, *Adv. Mater.*, 2019, **31**, 1902328.

26 L. Sun, W. Zhu, F. Yang, B. Li, X. Ren, X. Zhang and W. Hu, Molecular cocrystals: Design, charge-transfer and optoelectronic functionality, *Phys. Chem. Chem. Phys.*, 2018, **20**, 6009–6023.

27 D. Yan, A. Delori, G. O. Lloyd, T. Friščić, G. M. Day, W. Jones, J. Lu, M. Wei, D. G. Evans and X. Duan, A cocrystal strategy to tune the luminescent properties of stilbene-type organic solid-state materials, *Angew. Chem., Int. Ed.*, 2011, **50**, 12483–12486.

28 B. Zhou, Q. Zhao, L. Tang and D. Yan, Tunable room temperature phosphorescence and energy transfer in ratiometric co-crystals, *Chem. Commun.*, 2020, **56**, 7698–7701.

29 Q. Chen, X. Chen, Y. Han, T. Zhang, C.-P. Li, J. Mu, J. Zhang, J. Hao and P. Xue, Multistimuli-Responsive Fluorescent Switches Based on Reversible Decomposition and Regeneration of charge-transfer Complexes, *Cryst. Growth Des.*, 2022, **22**, 693–702.

30 Y. Liu, A. Li, S. Xu, W. Xu, Y. Liu, W. Tian and B. Xu, Reversible Luminescent Switching in an Organic Cocrystal: Multi-Stimuli-Induced Crystal-to-Crystal Phase Transformation, *Angew. Chem., Int. Ed.*, 2020, **59**, 15098–15103.

31 S. Wang, W. Xiang, C. Pan, J. Chen, W. Li, J. Zhang, J. Zhao and G. Liu, Changes in piezochromic luminescence of a charge transfer complex subjected to grinding and isotropic compression, *CrystEngComm*, 2023, **25**, 3861–3865.

32 S. Ito, C. Nishimoto and S. Nagai, Sequential halochromic/mechanochromic luminescence of pyridyl-substituted solid-state emissive dyes: thermally controlled stepwise recovery of the original emission color, *CrystEngComm*, 2019, **21**, 5699–5706.

33 Y. Sun, Y. Ye, X. Hu, Y. Bai and C. Xie, Mechano-/seeding-triggered crystal-to-crystal phase transition in luminescent switching cocrystals, *Dyes Pigm.*, 2023, **215**, 111275.

34 A. A. Ganie and A. A. Dar, Water Switched Reversible Thermochromism in Organic Salt of Sulfonated Anil, *Cryst. Growth Des.*, 2021, **21**, 3014–3023.

35 I. Ahmad and A. A. Dar, Switching the Solid-State Emission of Organic Crystals through Coformer Choice and Vapochromism, *J. Phys. Chem. C*, 2023, **127**, 18684–18693.

36 J. S. Zambounis, Z. Hao and A. Iqbal, Latent pigments activated by heat, *Nature*, 1997, **388**, 131–132.

37 Y. Chen, J. Li and J. Gong, Jumping Crystal Based on an Organic Charge Transfer Complex with Reversible ON/OFF Switching of Luminescence by External Thermal Stimuli, *ACS Mater. Lett.*, 2021, **3**, 275–281.

38 S. Das, L. Catalano and Y. Geerts, Gas Release as an Efficient Strategy to Tune Mechanical Properties and Thermoresponsiveness of Dynamic Molecular Crystals, *Small*, 2024, 2401317.

39 S. Li and D. Yan, Tuning Light-Driven Motion and Bending in Macroscale-Flexible Molecular Crystals Based on a Cocrystal Approach, *ACS Appl. Mater. Interfaces*, 2018, **10**, 22703–22710.

40 S. Li, B. Lu, X. Fang and D. Yan, Manipulating Light-Induced Dynamic Macro-Movement and Static Photonic Properties within 1D Isostructural Hydrogen-Bonded Molecular Cocrystals, *Angew. Chem., Int. Ed.*, 2020, **59**, 22623–22630.

41 A. Navarro-Huerta, M. J. Jellen, J. Arcudia, S. J. Teat, R. A. Toscano, G. Merino and B. Rodríguez-Molina, Tailoring the cavities of hydrogen-bonded amphidynamic crystals using weak contacts: towards faster molecular machines, *Chem. Sci.*, 2021, **12**, 2181–2188.

42 S. Zeghada, G. Bentabed-Ababsa, O. Mongin, W. Erb, L. Picot, V. Thiéry, T. Roisnel, V. Dorcet and F. Mongin,

2-Aminobenzaldehyde, a common precursor to acridines and acridones endowed with bioactivities, *Tetrahedron*, 2020, **76**, 131435.

43 H. Koshima, Solid State Bimolecular Photoreaction in a Simple Polycrystalline Mixture of Acridine and Carbazole, *Mol. Cryst. Liq. Cryst. Sci. Technol., Sect. A*, 2001, **356**, 483–486.

44 U. Garg, Y. Azim, M. Alam, A. Kar and C. P. Pradeep, Extensive Analyses on Expanding the Scope of Acid–Aminopyrimidine Synthons for the Design of Molecular Solids, *Cryst. Growth Des.*, 2022, **22**, 4316–4331.

45 L. Bian, H. Zhao, H. Hao, Q. Yin, S. Wu, J. Gong and W. Dong, Novel Glutaric Acid Cocrystal Formation via Cogrinding and Solution Crystallization, *Chem. Eng. Technol.*, 2013, **36**, 1292–1299.

46 H. Zhu, S. Weng, H. Zhang, H. Yu, L. Kong, Y. Zhong, Y. Tian and J. Yang, A novel carbazole derivative containing fluorobenzene unit: aggregation-induced fluorescence emission, polymorphism, mechanochromism and non-reversible thermo-stimulus fluorescence, *CrystEngComm*, 2018, **20**, 2772–2779.

47 Y. Shen, J. Hou, Y. Liu, X. Wan, M. Bai, X. Jiang, W. Duan and F. Yan, Deep insight into the charge-transfer cocrystals: Decreasing structural overlap induced bathochromically shift emission, *Dyes Pigm.*, 2023, **215**, 111277.

48 E. A. Hernández-Morales, A. Colin-Molina, J. Arcudia, F. J. Hernández, M. Rodríguez, R. A. Toscano, R. Crespo-Otero, G. Merino and B. Rodríguez-Molina, Indolocarbazole as a Platform for Concatenated Crystalline Rotors, *Cryst. Growth Des.*, 2023, **23**, 6785–6794.

49 Q. Li and Z. Li, The Strong Light-Emission Materials in the Aggregated State: What Happens from a Single Molecule to the Collective Group, *Adv. Sci.*, 2017, **4**, 1600484.

50 J.-L. Bredas, Mind the gap!, *Mater. Horiz.*, 2014, **1**, 17–19.

51 M. Rivera, M. Dommett and R. Crespo-Otero, ONIOM(QM:QM′) Electrostatic Embedding Schemes for Photochemistry in Molecular Crystals, *J. Chem. Theory Comput.*, 2019, **15**, 2504–2516.

52 M. Rivera, M. Dommett, A. Sidat, W. Rahim and R. Crespo-Otero, fromage: A library for the study of molecular crystal excited states at the aggregate scale, *J. Comput. Chem.*, 2020, **41**, 1045–1058.

53 F. J. Hernández and R. Crespo-Otero, Excited state mechanisms in crystalline carbazole: the role of aggregation and isomeric defects, *J. Mater. Chem. C*, 2021, **9**, 11882–11892.

54 L. A. Rodríguez-Cortés, F. J. Hernández, M. Rodríguez, R. A. Toscano, A. Jiménez-Sánchez, R. Crespo-Otero and B. Rodríguez-Molina, Conformational emissive states in dual-state emitters with benzotriazole acceptors, *Matter*, 2023, **6**, 1140–1159.

55 S. Ma, S. Du, G. Pan, S. Dai, B. Xu and W. Tian, Organic molecular aggregates: From aggregation structure to emission property, *Aggregate*, 2021, **2**, e96.

56 C. F. Mackenzie, P. R. Spackman, D. Jayatilaka and M. A. Spackman, CrystalExplorer model energies and energy frameworks: Extension to metal coordination compounds, organic salts, solvates and open-shell systems, *IUCrJ*, 2017, **4**, 575–587.

57 M. A. Spackman, P. R. Spackman and S. P. Thomas, in *Complementary Bonding Analysis*, ed. S. Grabowsky, D. Gruyter, 2021, pp. 329–352.

58 A. Lemmerer, D. A. Adsmond, C. Esterhuysen and J. Bernstein, Polymorphic Co-crystals from Polymorphic Co-crystal Formers: Competition between Carboxylic Acid···Pyridine and Phenol···Pyridine Hydrogen Bonds, *Cryst. Growth Des.*, 2013, **13**, 3935–3952.

59 P. P. Mazzeo, S. Canossa, C. Carraro, P. Pelagatti and A. Bacchi, Systematic coformer contribution to cocrystal stabilization: energy and packing trends, *CrystEngComm*, 2020, **22**, 7341–7349.

60 M. Mirzaei, F. Sadeghi, K. Molčanov, J. K. Zaręba, R. M. Gomila and A. Frontera, Recurrent Supramolecular Motifs in a Series of Acid-Base Adducts Based on Pyridine-2,5-Dicarboxylic Acid N-Oxide and Organic Bases: Inter- And Intramolecular Hydrogen Bonding, *Cryst. Growth Des.*, 2020, **20**, 1738–1751.

61 N. Bedeković, V. Stilinović and T. Piteša, Aromatic versus Aliphatic Carboxyl Group as a Hydrogen Bond Donor in Salts and Cocrystals of an Asymmetric Diacid and Pyridine Derivatives, *Cryst. Growth Des.*, 2017, **17**, 5732–5743.

62 A. Navarro-Huerta, D. A. Hall, J. Blahut, V. Gómez-Vidales, S. J. Teat, J. M. Marmolejo-Tejada, M. Dračínský, M. A. Mosquera and B. Rodríguez-Molina, Influence of Internal Molecular Motions in the Photothermal Conversion Effect of Charge-Transfer Cocrystals, *Chem. Mater.*, 2023, **35**, 10009–10017.

63 P. Gayathri, M. Pannipara, A. G. Al-Sehemi and S. P. Anthony, Triphenylamine-based stimuli-responsive solid state fluorescent materials, *New J. Chem.*, 2020, **44**, 8680–8696.